Ultrastructural analysis of wild-type and RIM1α knockout active zones in a large cortical synapse
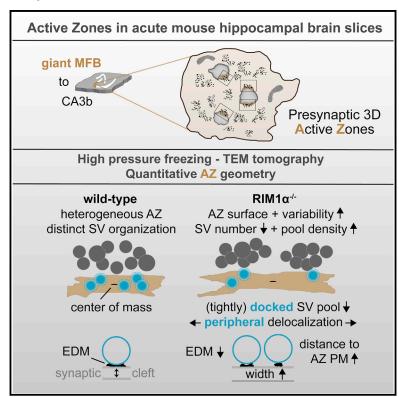
Graphical abstract

Authors

Katharina Lichter, Mila Marie Paul, Martin Pauli, ..., Christian Stigloher, Manfred Heckmann, Anna-Leena Sirén

Correspondence

christian.stigloher@uni-wuerzburg.de (C.S.),
heckmann@uni-wuerzburg.de (M.H.),
anna-leena.siren@uni-wuerzburg.de (A.-L.S.)

In brief

Applying electron tomography on high-pressure frozen acute brain slices, Lichter et al. investigate the 3D near-to-native ultrastructure of presynaptic active zones in hippocampal mossy fiber synapses in wild-type and RIM1α knockout mice. Besides its role in tight vesicle docking, RIM1α is crucial for synaptic architecture and vesicle pool organization.

Highlights

- Near-to-native AZ ultrastructure in hippocampal MFBs is altered in absence of RIM1α

- RIM1α deletion increases the AZ surface area and synaptic cleft width

- RIM1α deletion influences number, structure, and position of tightly docked SVs

- RIM1α deletion leads to a heterogeneous SV pool organization

CellPress

Report

Ultrastructural analysis of wild-type and RIM1α knockout active zones in a large cortical synapse

Katharina Lichter,[1,2,3] Mila Marie Paul,[2,4] Martin Pauli,[2] Susanne Schoch,[5] Philip Kollmannsberger,[6] Christian Stigloher,[7,*] Manfred Heckmann,[2,*] and Anna-Leena Sirén[1,2,8,*]

[1]Department of Neurosurgery, University Hospital of Würzburg, 97080 Würzburg, Germany
[2]Institute for Physiology, Department of Neurophysiology, Julius-Maximilians-University Würzburg, 97070 Würzburg, Germany
[3]Center of Mental Health, Department of Psychiatry, Psychosomatics and Psychotherapy, University Hospital of Würzburg, 97080 Würzburg, Germany
[4]Department of Orthopedic Trauma, Hand, Plastic and Reconstructive Surgery, University Hospital of Würzburg, 97080 Würzburg, Germany
[5]Department of Neuropathology and Department of Epileptology, University Hospital Bonn, 53127 Bonn, Germany
[6]Center for Computational and Theoretical Biology, Julius-Maximilians-University Würzburg, 97074 Würzburg, Germany
[7]Imaging Core Facility, Biocenter, University of Würzburg, 97074 Würzburg, Germany
[8]Lead contact
*Correspondence: christian.stigloher@uni-wuerzburg.de (C.S.), heckmann@uni-wuerzburg.de (M.H.), anna-leena.siren@uni-wuerzburg.de (A.-L.S.)
https://doi.org/10.1016/j.celrep.2022.111382

SUMMARY

Rab3A-interacting molecule (RIM) is crucial for fast Ca^{2+}-triggered synaptic vesicle (SV) release in presynaptic active zones (AZs). We investigated hippocampal giant mossy fiber bouton (MFB) AZ architecture in 3D using electron tomography of rapid cryo-immobilized acute brain slices in RIM1α$^{-/-}$ and wild-type mice. In RIM1α$^{-/-}$, AZs are larger with increased synaptic cleft widths and a 3-fold reduced number of tightly docked SVs (0–2 nm). The distance of tightly docked SVs to the AZ center is increased from 110 to 195 nm, and the width of their electron-dense material between outer SV membrane and AZ membrane is reduced. Furthermore, the SV pool in RIM1α$^{-/-}$ is more heterogeneous. Thus, RIM1α, besides its role in tight SV docking, is crucial for synaptic architecture and vesicle pool organization in MFBs.

INTRODUCTION

Rab3A-interacting molecules (RIMs) form evolutionarily conserved, presynaptic scaffold complexes at the active zone (AZ) mesoscale (Emperador-Melero and Kaeser, 2020; Goodsell et al., 2020). In vertebrates and invertebrates, RIMs and homologues facilitate synaptic transmission and information storage (Castillo et al., 2002; Kintscher et al., 2013; Müller et al., 2012; Paul et al., 2022; Schoch et al., 2002; Stigloher et al., 2011).

RIM contains five core protein domains (Zinc finger, PDZ, C$_2$A, PxxP, C$_2$B). Via the N-terminal Zinc finger it binds to Rab3A (Wang et al., 1997), Munc13-1 (Andrews-Zwilling et al., 2006; Deng et al., 2011), and via PxxP to the scaffold protein RIM-BP (Hibino et al., 2002; Wang et al., 2002). Its PDZ-, C$_2$A-, and C$_2$B-domain bind to P/Q- and N-type voltage gated calcium channels (VGCCs) (Deng et al., 2011; Han et al., 2011; Kaeser et al., 2011, 2012; Kiyonaka et al., 2007; Miki et al., 2007). RIM C$_2$B-domain interacts with the presynaptic membrane (de Jong et al., 2018) and liprin-α3 (Schoch et al., 2002).

On an ultrastructural level, electron microscopic (EM) investigations of RIM1α deficiency showed a reduction of the docked SV pool and SV tethering in rapid-cryoimmobilized synaptosomal preparations of mouse cortical neurons (Fernandez-Busnadiego et al., 2013). RIM1α is the major RIM isoform in the hippocampal mossy fiber/CA3 region (Schoch et al., 2006). Within the tri-synaptic hippocampal circuit, the morphologically diverse giant mossy fiber bouton (MFB)-to-pyramidal CA3 neuron synapses function as "conditional" detonators to time and control downstream postsynaptic activity (Amaral and Dent, 1981; Galimberti et al., 2006; Hallermann et al., 2003; Henze et al., 2002; Lawrence et al., 2004; Rollenhagen et al., 2007; Wilke et al., 2013; Zhao et al., 2012). Giant MFB synapses are characterized by a large pool of release-ready SVs, low release probability, and loose coupling distance between VGCC and Ca^{2+} sensor (Hallermann et al., 2003; Jonas et al., 1993; Lawrence et al., 2004; Vyleta and Jonas, 2014). To further clarify the molecular architecture of synaptic connections in giant MFBs and their complex SV pools, we used systematic, highly standardized electron tomography for 3D ultrastructural quantification of near-to-native synapses in rapid cryo-immobilized acute hippocampal slices of male adult RIM1α$^{-/-}$ mice and age-matched wild-type littermates. We answer the following questions:

1. Do the size of giant MFB AZs and the synaptic cleft width depend on RIM1α?
2. Are number and position of docked SVs influenced by RIM1α and is the electron-dense material (EDM) connecting docked vesicles with presynaptic membrane altered?
3. Is the organization of the synaptic SV pool changed at RIM1α$^{-/-}$ AZs?
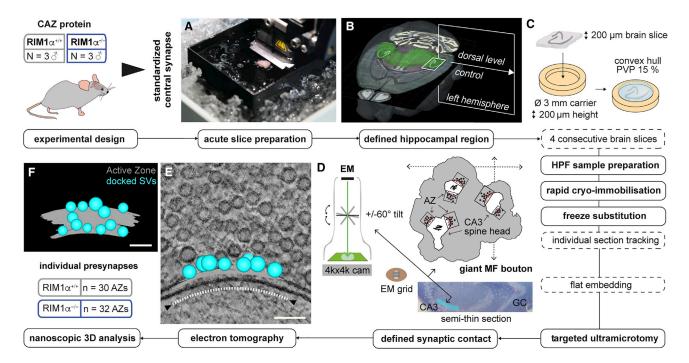
Figure 1. Schematic workflow for standardized ultrastructural analysis of presynapses in giant hippocampal MF boutons

(A) Young male adult wild-type (RIM1α$^{+/+}$, gray, n = 3) and RIM1α knockout mice (RIM1α$^{-/-}$, blue, n = 3) were used for systematic analysis of three-dimensional active zone (AZ) ultrastructure in standardized giant hippocampal MFB synapses to decipher morphological phenotypes of cytomatrix AZ proteins (CAZ). After decapitation, brains were removed immediately for acute slicing in artificial cerebrospinal fluid (ACSF) using a vibratome.

(B) Horizontal section from Allen Mouse Brain Atlas illustrates the region of interest in the dorsal left hippocampus from which at least four consecutive 200-μm-thick brain slices were obtained.

(C) Slices were transferred in high-pressure freezing (HPF) carriers of 3 mm diameter and 200 μm height (Type A) filled with PVP 15% as cryoprotectant.

(D) Summary of sample processing including rapid cryo-immobilization, freeze substitution, and targeted ultramicrotomy for electron tomography of defined synaptic contacts (AZ, black box) of giant hippocampal MFBs (gray) at spiny excrescences/spine heads, containing spine apparatus, of CA3b pyramidal neurons (cyan shading in methylene blue stained semithin section).

(E) Reconstructed electron tomographic subvolume of a MF synaptic contact. Presynaptic 3D AZ surface (gray), defined as the presynaptic membrane opposite to the postsynaptic membrane at which postsynaptic filaments are densely connected (extent indicated by dotted line between black arrowheads), and docked synaptic vesicles (SVs, cyan) are highlighted.

(F) Ultrastructural 3D analysis of synaptic contacts of an individual giant MFB on average on 466 2D AZ profiles/synaptic contact in 30 RIM1α$^{+/+}$AZs (10/mouse) and 398 2D AZ profiles/synaptic contact in 32 RIM1α$^{-/-}$ AZs (10–12/mouse) was performed with ETomo/IMOD and Python software packages. Experimental workflow and analysis were performed blinded to the genotype. See also Figure S1. Scale bars, (E and F) 100 nm.

RESULTS

Targeted cutting for imaging of giant MFB AZs

MFB AZs are highly heterogeneous within the mossy fiber (MF) tract and along the dorsoventral hippocampal axis (Kheirbek et al., 2013; Pauli et al., 2021). We used a standardized protocol for ultrastructural AZ analysis of brains of three male RIM1α$^{-/-}$ and three wild-type littermates to prepare acute slices of the left dorsal hippocampus (Figures 1A and 1B). To avoid fixative induced alterations of AZ architecture (Korogod et al., 2015; Weimer, 2006; Zhao et al., 2012), rapid cryo-immobilization and freeze substitution were applied (Figure 1C). We used targeted ultramicrotomy to clearly identify supra-pyramidal giant hippocampal MFB synapses to spiny excrescences/spine heads of CA3b pyramidal neurons (Figure 1D). EM tomography was carried out on 250-nm semi-thin hippocampal resin sections in high resolution and magnification (Figure 1D) to obtain a 3D morphological dataset for analysis of MFB AZs (Figures 1E and

1F). Giant MFB AZs were defined as presynaptic compartments containing dense SV clusters including docked SVs in near proximity to and at the presynaptic AZ membrane. The presynaptic 2D AZ profile and 3D AZ surface, respectively, were defined by their localization opposite to the postsynaptic membrane at which electron-dense postsynaptic filaments (PSF) were densely connected. Pre- and postsynaptic compartments were separated by the synaptic cleft, a characteristic widening between both membranes containing a network of electron-dense filaments. All EM tomograms of AZs were reconstructed with a fiducial free patch tracking protocol and annotated as individual IMOD models (Figure S1, Table S1B).

AZ surface area and synaptic cleft width are increased in RIM1α$^{-/-}$

We identified the characteristic morphology of giant MFBs (Maus et al., 2020; Rollenhagen et al., 2007; Wilke et al., 2013; Zhao et al., 2012), including a dense filling with SVs of different type
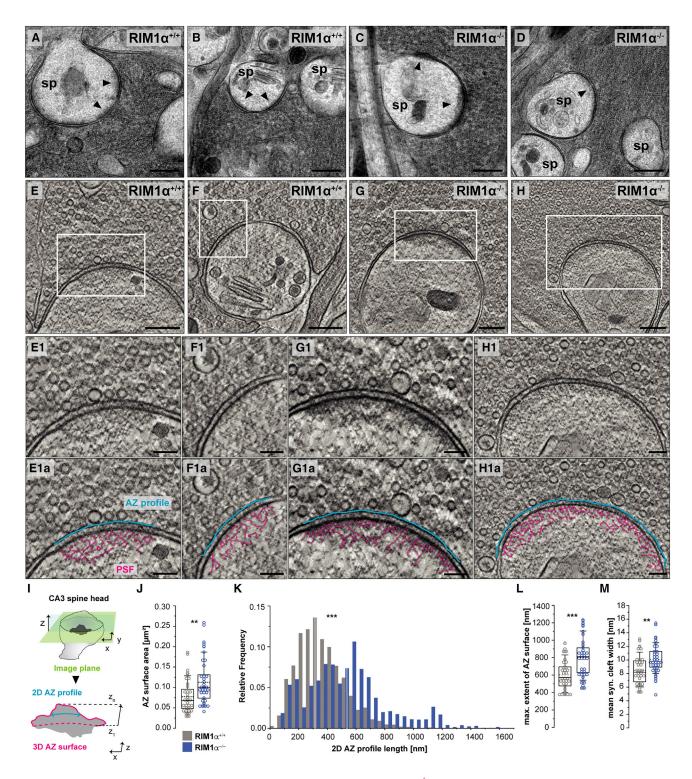
Figure 2. Ultrastructural 3D analysis reveals larger hippocampal MFB AZs in RIM1α−/− mice

(A–D) Exemplary EM micrographs of 250-nm semithin tissue sections show overviews of giant MFBs in the CA3b region within the left dorsal hippocampus of RIM1α+/+ (A and B) and RIM1α−/− mice (C and D). Black arrowheads in spine heads (sp) of CA3b neurons highlight postsynaptic membranes with dense and asymmetric PSF. Individual AZs at the opposite presynaptic membrane were used for EM tomography.

(E–H) Selected EM tomographic slices of individual hippocampal MFBs (Figures 2A–2D) in RIM1α+/+ (E and F) and RIM1α−/− (G and H). White boxes highlight AZs enlarged in E1–H1.

(legend continued on next page)

(clear SVs with various diameter, dense-core SVs) and the existence of spiny excrescences/spine heads within the boutons itself (Figures 2A–2D). In giant MFBs, one or more AZs were localized at spine heads that partially contained spine apparatus (Figures 2E–2H). For EM tomography, clearly defined 2D AZ profiles with intact membranes (Figures 2E1-H1, Figures 2E1a-H1a), one individual AZ of each giant MFB, were selected; for segmentation and annotation, only EM tomograms of AZs were included in which pre- and postsynaptic membranes were distinguishable and viewable throughout the entire image volume.

RIM1α$^{-/-}$ giant MFB to CA3b spine head AZ surface areas were significantly larger than wild-type AZ surface areas (Figures 2I and 2J, see Table S1 for all numerical and statistical values not stated in the text). In both genotypes, AZ surface areas between individual animals showed no statistical difference (Figure S2A). Larger RIM1α$^{-/-}$ giant MFB AZ surface areas were independent of inter-animal variability (Figures S2B–S2E, Table S1C). The observed increase of area in RIM1α$^{-/-}$ giant MFB AZs was robust and highly significant compared with RIM1α$^{+/+}$ in estimation statistics based on the available data (linear mixed modeling, bootstrapping, Figures S2B–S2E, Table S1C). Two-dimensional area of CA3b pyramidal neuron spine heads showed no statistical difference between genotypes (Figures S2F–S2G).

The distribution of 2D presynaptic AZ profile lengths in individual EM tomograms of all included AZs, was more variable in RIM1α$^{-/-}$ (Figure 2K). Next, we determined the maximum spatial extent of individual AZ surfaces in 3D, which was also significantly increased in RIM1α$^{-/-}$ mice from 602.3 nm in wild-type to 802.5 nm in RIM1α$^{-/-}$ (Figure 2L).

We three-dimensionally annotated the entire synaptic cleft volume of individual synapses, which was defined by both the extent of the AZ surfaces and PSF. By normalizing the synaptic cleft volume to the respective AZ surface area, a mean width for the entire synaptic cleft was calculated instead of a single 2D measurement. The width of the synaptic cleft was increased in RIM1α$^{-/-}$ compared with wild-type mice (Figure 2M). The synaptic cleft width appeared largest in the synapse center and narrowed toward the edges and depended on the curvature of the spine head membranes.

The percentage of mitochondrial network near the AZ and the perisynaptic zone was higher in RIM1α$^{-/-}$ (Figures S3A and S3B). To quantify this, we used a 2D spatial stereology with a systematic grid lattice and at defined magnification (Figure S3C). The total mitochondrial area within 100–500 nm of the AZ membrane and its perisynaptic zone was increased in RIM1α$^{-/-}$ AZs compared with wild-type (Figures S3D and S3E).

Reduction of the docked SV pool and diminution of the SV-attached EDM at RIM1α$^{-/-}$ AZs

We individually analyzed at high magnification all SVs within 0–10 nm of the AZ membrane (Figure 3A, Video S1) covering the range of the SNARE proteins. SVs situated within 0 to 2-nm distance to the presynaptic membrane with prominent EDM connecting the SV with the presynaptic membrane were defined as "tightly docked." In RIM1α$^{-/-}$, tightly docking was greatly reduced (Figure 3B). Since previous studies differ in the definition of docked SVs (Borges-Merjane et al., 2020; Neher and Brose, 2018; Rothman et al., 2017; Tang et al., 2016), we defined "docked" for all SVs connected to the presynaptic membrane within 0 to 5-nm distance. Here, the number of docked SVs in RIM1α$^{-/-}$ AZs was also reduced compared with wild-type AZs (Figure 3B). In both genotypes we observed few AZs without any tightly docked SVs (wild-type 1 AZ, RIM1α$^{-/-}$ 5 AZs) and without any docked SVs (wild-type 1 AZ, RIM1α$^{-/-}$ 6 AZs, Table S1B). We found no difference of docked SV numbers within 2.1 to 5-nm distance (Figure 3B), and, thus, attribute the significant difference in docking to the tightly docked SV pool. Furthermore, SV numbers within 5 to 10-nm distance from the membrane, where SVs are tethered to the membrane via EDMs (Fernandez-Busnadiego et al., 2013), were unchanged (Figure 3B). Interestingly, SVs within the 0 to 10-nm zone were nearly 2-fold farther from the AZ membrane in RIM1α$^{-/-}$ than in wild-type.

We also quantified SVs that were localized at less than 10-nm distance to the perisynaptic membrane (within 200 nm of the AZ edges) (Figure 3C). In both genotypes, we rarely detected SVs in a tethered or docked status outside of the AZ. The median distance of such SVs to the perisynaptic membrane was significantly higher in RIM1α$^{-/-}$ (Figure 3C).

In view of the differences in docked SV numbers and mean distance of SVs to the membrane between the genotypes, we analyzed the morphology of the EDM connecting docked SVs and the AZ membrane (Harlow et al., 2001). We analyzed EDM width for docked SVs in electron tomographic slices dissecting the SV center at high resolution. Although our near-to-native tissue preparation and 3D tomogram reconstruction facilitated detection of thin electron-dense filaments on the SV surface (Figure 3, Video S1), annotation of individual filaments remains highly subjective. Thus, we focused on the longest continuous part of the EDM that was parallelly orientated to the presynaptic AZ membrane profile (Figure 3D). In RIM1α$^{-/-}$ AZs, the EDM connecting tightly docked SVs with the presynaptic membrane is smaller compared with

(E1–H1) Enlarged view indicated by white boxes in E–H show presynaptic AZs of hippocampal MFBs in RIM1α$^{+/+}$ (E1 and F1) and RIM1α$^{-/-}$ mice (G1 and H1). In E1a–H1a, PSF (magenta) at the postsynaptic membrane and the directly opposite presynaptic membrane as 2D AZ profile (blue) are exemplarily highlighted for illustrative purposes.

(I) Illustration of selected image plane (green) for visualization of presynaptic MF AZs at CA3 spine heads. Measurements of AZ surface and AZ profile are indicated below.

(J) Summary graphs of AZ surface area (p = 0.002) in RIM1α+/+ (gray, n = 30 AZs, three animals) and RIM1α$^{-/-}$ (blue, n = 32 AZs, three animals). See also Figure S2. Throughout this manuscript, horizontal lines in boxplots represent median; boxes quartiles; whiskers 10th and 90th percentiles; scatter plots show individual data points for each group. Asterisks indicate significance level (*p < 0.05, **p < 0.01, ***p < 0.001).

(K) Histograms of 2D AZ profile lengths (p < 0.001) obtained from all analyzed tomograms show broader distribution in RIM1α$^{-/-}$ (n = 12,750 AZ profile lengths) than RIM1α$^{+/+}$ (n = 13,991 AZ profile lengths). Medians are indicated as white lines in histogram bins throughout the manuscript.

(L and M) Summary graphs of the maximal AZ extent (L, p < 0.001) obtained and synaptic cleft width (M, p = 0.002) calculated based on IMOD models in both groups. Scale bars, (A–D) 250 nm, (E–H) 250 nm, (E1–H1) 100 nm.
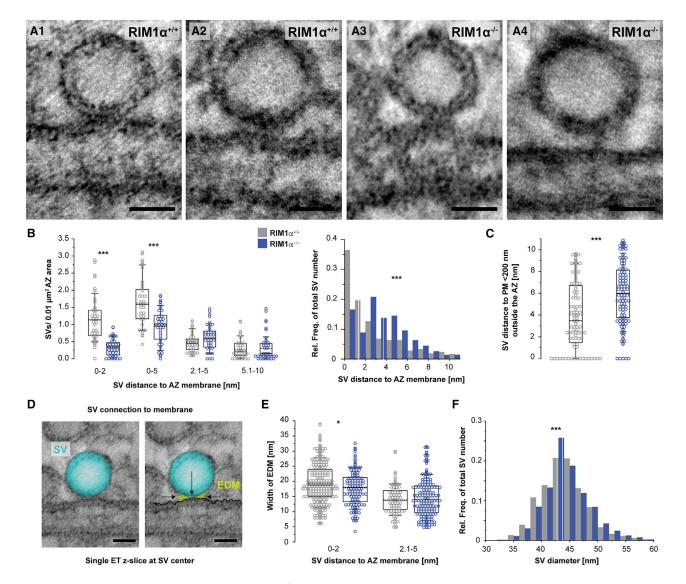
Figure 3. Altered docking of synaptic vesicles at RIM1α−/− giant MFB AZs

(A) EM tomographic slices of individual SVs depicted at their centers at the presynaptic membrane in RIM1α+/+ (A1 and A2) and RIM1α−/− (A3 and A4). See also Video S1.

(B) Summary graphs of normalized SV numbers within 0–2-nm (p < 0.001), 0–5-nm (p < 0.001), 2.1–5-nm (p = 0.123), and 5.1–10-nm (p = 0.871) distance to the AZ membrane in RIM1α+/+ (gray) and RIM1α−/− (blue) and histograms of the distance distribution of SVs and the AZ membrane within 0–10 nm.

(C) Summary graph of outer docked and tethered SVs (i.e., < 200 nm to AZ edges) within 0–10-nm distance to the AZ membrane in both groups (p < 0.001).

(D) Visualization of a 3D docked SV (cyan) at its center with electron-dense material (EDM, green) connecting SV and the AZ membrane in an electron tomographic slice in front view. EDM width was measured at its longest continuous part indicated by two opposite black arrows.

(E) The maximal EDM width in tightly docked SVs decreases in RIM1α−/− AZs compared with RIM1α+/+ (p = 0.033). SVs of 2.1–5-nm distance, connected via EDM to the AZ membrane, do not differ in their maximal EDM width (p = 0.665). See also Figure S4A.

(F) SVs in the total SV pool (0–200 nm) annotated per tomogram have an increased diameter in RIM1α−/− AZs compared with RIM1α+/+ (p < 0.001). Scale bars, (A1–A4, D) 25 nm.

wild-type AZs (Figure 3E). EDM widths of SVs connected to the membrane in 2.1 to 5-nm distance did not differ (Figure 3E); however, the quantified EDM was significantly smaller in both genotypes compared with tightly docked SVs (Figure S4A, p < 0.001). Normalized calculations of the EDM to its corresponding SV diameter further supported these findings (Figure S4A). The overall diameter of SVs within 0 to 200-nm in RIM1α−/− was larger compared with wild-type SVs (cutoff for SV radius: 30 nm, Figure 3F).

Delocalization of the tightly docked SV pool in RIM1α−/−

We systematically profiled individual tightly docked SVs upon their five nearest neighboring docked SVs, their position to both AZ edges in the EM tomogram, and their distance to the
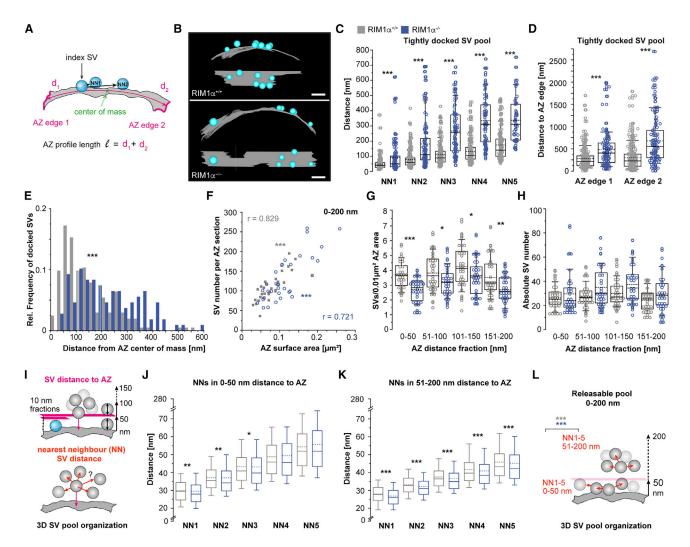
Figure 4. Spatial delocalization of different synaptic vesicle pools in RIM1α$^{-/-}$ giant MFB synapses

(A) Visualization of standardized distance measurements for the tightly docked SV pool at giant MFB AZs. The tightly docked index SV (cyan) is localized to the five nearest neighboring tightly docked SVs at the AZ membrane. Further, the position of the index SV within the AZ is computed via its distances (d$_1$, d$_2$) to corresponding AZ edges (magenta) and the 3D AZ center of mass (c.o.m.).

(B) Exemplary IMOD models of the tightly docked SV pool at the AZ membrane of giant MFB AZs in RIM1α$^{+/+}$ and RIM1α$^{-/-}$ animals.

(C) Individual neighboring tightly docked SVs are wider distributed at the AZ membranes in RIM1α$^{-/-}$ AZs than in controls (p < 0.001).

(D) Individual docked SVs in RIM1α$^{+/+}$ show an increased absolute distance to both corresponding AZ edges compared with RIM1α$^{+/+}$ (p < 0.001). See also Figure S4B.

(E) The distance of docked SVs to the AZ c.o.m. is increased and widely distributed in RIM1α$^{-/-}$ AZs compared with RIM1α$^{+/+}$ (p < 0.001).

(F) Positive Spearman correlation coefficient of the total SV number in 0–200-nm distance to the presynaptic membrane and the area of individual AZs in RIM1α$^{+/+}$ (gray, r = 0.829, p < 0.001) and RIM1α$^{-/-}$ (blue, r = 0.721, p < 0.001) mice.

(G–H) Summary graphs of normalized SV numbers (G) and absolute SV numbers (H) within 0–50-nm (p < 0.001), 51–100-nm (p = 0.043), 101–150-nm (p = 0.037), and 151–200-nm distance (p = 0.007) to the AZ membrane in both groups.

(I) Illustration of 2D and 3D SV pool organization analyses in 2D distance fractions of 10 or 50-nm distance from the AZ membrane (upper panel) and using 3D nearest neighbor analysis (NN, lower panel).

(J–K) Summary graphs of the distance from the AZ membrane for NN1-5 within 0–50 nm (NN1: p = 0.004, NN2: p = 0.003, NN3: p = 0.038, NN4: p = 0.820, NN5: p = 0.720), and 51–200 nm (F, NN1-5: p < 0.001) to the AZ.

(L) 3D illustration of the recycling pool: NN1-5 SV pool distances within 0–50-nm and 51–200-nm distance to the AZ membrane significantly differ in both genotypes (RIM1α$^{+/+}$: p < 0.001, RIM1α$^{-/-}$: p < 0.001). Scale bar, (B) 100 nm.

3D center of mass (c.o.m.) of the AZ (Figures 4A and 4B) (Butola et al., 2021; Kusick et al., 2020). In RIM1α$^{-/-}$ AZs, the distance of the tightly docked index SV to its five nearest neighboring tightly docked SVs is largely increased compared with controls (Fig-

ure 4C and Table S1). Using the 2D AZ profile length as a reference of the tightly docked SV position (Figure 4A and (Kusick et al., 2020), the distance of the projected SV center onto the AZ profile to both corresponding edges was larger in RIM1α$^{-/-}$

(Figures 4B and 4D). To account for the huge increase of AZ surface area in RIM1$\alpha^{-/-}$, the calculations were further normalized to the corresponding 2D AZ profile length (Figure 4A) and the ratio of both distances was compared (Figure S4B). Tightly docked SVs in RIM$\alpha^{-/-}$ AZs are localized nearer the AZ edges than in controls (Figures 4D and S4). Tightly docked SVs in wild-type AZs are located closer to the AZ c.o.m. (Figure 4D). As giant MFB AZs are complex in 3D, the c.o.m. of the AZ is one possible standardization to report spatial differences (Mrestani et al., 2021). The distance of an individual tightly docked SV to the 3D c.o.m. of the AZ was increased nearly 2-fold in RIM1$\alpha^{-/-}$ compared with wild-type (Figure 4E).

Heterogeneous distribution of SVs within the pool up to 200 nm in RIM1$\alpha^{-/-}$

The tightly docked SV pool of giant MFB AZs is largely re-organized in the absence of RIM1α. Is this associated with a reduced synaptic SV pool? The SV pool size per annotated AZ, defined as all SVs within a 200-nm euclidean distance to the presynaptic membrane, positively correlated with the surface area of RIM1$\alpha^{-/-}$ and wild-type AZs (F = 1.699, p = 0.192, F-test; Figure 4F). At 0 to 50-nm distance to the presynaptic membrane, this correlation was still present; however, correlation strength was decreased in RIM1$\alpha^{-/-}$ (Table S1A). In RIM1$\alpha^{-/-}$ MFB AZs, the SV pool within the 200-nm distance to AZ was reduced (Table S1A). Taking into account the median SV diameter of 43 to 44 nm at giant MFB AZs plus a zone of SV proteins on the outer SV membrane, it is reasonable to differentiate the SV pool in 2D distance fractions of 50 nm (Kaeser and Regehr, 2017). In RIM1$\alpha^{-/-}$ giant MFB AZs, all four 50-nm distance fractions (first fraction: 0–50 nm, 2nd fraction: 51–100 nm, 3rd fraction: 101–150 nm, 4th fraction: 151–200 nm) showed a significant reduction in SV number per 0.01 μm^2 AZ area (Figure 4G). In both genotypes, most SVs were found within the third 50-nm distance fraction (Figure 4G).

We next performed the nearest neighbor (NN) analysis of surrounding SVs in 0 to 50-nm and 51 to 200-nm distance to the presynaptic AZ membrane (Figure 4H). In the first 50-nm distance fraction, NN 1–3 distances were smaller in the RIM1$\alpha^{-/-}$ SV pool (Figure 4I). In the farther 50-nm distance fractions, even NN 1–5 distances were smaller (Figure 4J). Interestingly, the overall NN distance in the second to fourth 50-nm distance fraction was significantly smaller than in the first 50-nm distance fraction (for both genotypes: p < 0.001, Mann-Whitney Rank Sum Test, Figure 4K).

DISCUSSION

The present study provides a quantitative 3D analysis of AZ ultrastructure in giant MFBs using electron tomography of rapid cryo-immobilized acute brain slices. Since RIM1α is the major isoform of RIM proteins in MFBs (Schoch et al., 2006), we concentrated on AZ ultrastructure in giant MFB to CA3b spine head synapses of adult male RIM1α knockout and wild-type littermates instead of RIM1/2 knockout mice (Kaeser et al., 2011). Moreover, cryo-EM tomography of cortical synaptosomes of RIM1$\alpha^{-/-}$ mice revealed a critical role of RIM1α for SV tethering (Fernandez-Busnadiego et al., 2013). However, the role of RIM1α for defined AZs

and their SV pools of hippocampal giant MFBs in cryo-immobilized acute brain slices has not been investigated so far.

From a general perspective, our wild-type data of MFB AZs in acute brain slices such as AZ profile length, SV diameter, number of tightly docked SVs, and the percent occupancy of AZ surface area with mitochondria fit with recent electron tomographic data from hippocampal organotypic slice cultures (Maus et al., 2020). Previous studies have described diverse changes in SV docking and AZ ultrastructure after induction of plasticity in giant MFB synapses (Borges-Merjane et al., 2020; Imig et al., 2020; Maus et al., 2020; Orlando et al., 2021; Zhao et al., 2012), but there still is a need for quantitative data on AZ geometry in clearly defined giant MFB synaptic contacts.

RIM1$\alpha^{-/-}$ AZs in giant MFBs showed an expansion of area surface and synaptic cleft, reduced docked SV pools, and modified SV docking apparatus, lateralization of tightly docked SVs toward the AZ edge, and a distinctly altered SV pool organization up to 200-nm distance to the presynaptic membrane. These findings imply that RIM1α is essential for a complex AZ ultrastructure and SV arrangement in giant MFBs.

AZ surface size and synaptic cleft width depend on RIM1α

We found a striking increase of 3D AZ surface size and maximum extent as well as 2D AZ profile length in the MFB to CA3 spine head synapses in RIM1$\alpha^{-/-}$. These data are in accordance with findings reported in cryo-immobilized cortical synaptosomal preparations (Fernandez-Busnadiego et al., 2013). By targeted cutting and focusing on one defined synapse type, we obtained highly standardized data. Nevertheless, the AZ dimensions showed remarkable variability in wild-type which was further augmented in RIM1$\alpha^{-/-}$. On average, AZ surface area increased by 30% in RIM1$\alpha^{-/-}$. Furthermore, the shape of an individual AZ showed a high complexity (Figures 2K and S1) which is in line with other studies (Pauli et al., 2021; Zhao et al., 2012). This complexity was further increased in RIM1$\alpha^{-/-}$. In view of the observed changes in AZ dimensions, molecular interactions of the multidomain protein RIM1α should be considered. Several RIM1α domains bind to VGCCs and its Zinc finger domain to SVs, therefore RIM is an essential link (Kaeser et al., 2011; Schoch et al., 2002). In addition, RIM1α interacts with core AZ components like ELKS/CAST, RIM-BP, and α-liprin, generating a multifunctional scaffold (Emperador-Melero and Kaeser, 2020). Therefore, the absence of RIM1α results in a disassembly of AZ scaffold leading to an increase in AZ surface area and variability. Although our EM tomography technic does not allow molecular mapping of individual proteins such as VGCCs and the above-named scaffold proteins in AZs, it appears likely that the observed increase in AZ surface area is accompanied by a redistribution of these components.

Since Castillo et al. (Castillo et al., 2002) mentioned no difference in 2D AZ profile length in MFBs between RIM1$\alpha^{-/-}$ and WT mice, the larger AZ surface area and the increase in synaptic cleft width in the RIM1$\alpha^{-/-}$ were unexpected. While the absolute difference in cleft width between wild-type and RIM1$\alpha^{-/-}$ was only 2 nm and theoretically still fits to simulated optimal widths maintaining synaptic strength (Savtchenko and Rusakov, 2007), the relative difference is 20%. However, the 20% change in 2D width translates to

much bigger cleft volume change in 3D and it is likely to be of relevance for synaptic transmission. Structurally, re-distributed AZ components and/or lost (indirect) interactions with postsynaptic receptors (Tang et al., 2016) or synaptic adhesion molecules, such as neurexin-1 (Brockhaus et al., 2018), may lead to alterations in the complex cleft ultrastructure (Martinez-Sanchez et al., 2021) or ultrastructure of transsynaptic nano-"columns" (Tang et al., 2016) in RIM1$\alpha^{-/-}$ giant MFB AZs. Functionally, it should be considered that larger synaptic cleft volumes in RIM1$\alpha^{-/-}$ may affect concentration and diffusion kinetics of neurotransmitter molecules and ions, e.g., specifically zinc in giant MFB synaptic clefts, resulting in altered synaptic currents. However, this mechanism does not seem to compromise overall synaptic function of giant MFB synapses (Castillo et al., 2002).

Number and position of SVs are influenced by RIM1α

We report substantial reduction of (tight) SV docking at giant MFB AZs in the absence of RIM1α. This supports the role of RIM in SV docking/priming and is consistent with findings in synaptosomal preparations (Fernandez-Busnadiego et al., 2013) and in dissociated hippocampal cultures of RIM1/2-deficient mice (Zarebidaki et al., 2020).

Tight SV docking is assumed to be mediated by an interaction of the Zinc finger of RIM with the C_2A domain of Munc13-1 (Imig et al., 2014; Neher and Brose, 2018). For the Zinc finger of RIM, it is proposed that it recruits Munc13 to the AZ (Andrews-Zwilling et al., 2006). Deletion of RIM1α lead to a 60% reduction of Munc13-1 expression (Andrews-Zwilling et al., 2006; Schoch et al., 2002). Mechanistically, the RIM Zinc finger is required for disruption of autoinhibitory homodimerization by forming a heteromeric complex with Munc13 (Deng et al., 2011). Thus, the reduced SV docking phenotype in RIM1$\alpha^{-/-}$ can be explained by these changes. Recent EM quantifications of SV docking associated the heterodimer of RIM/Munc13-1 with SV docking due to the formation of monomeric priming-competent Munc13 molecules (Camacho et al., 2017). A second explanation for reduced tight docking could be the reduction of the RIM C_2B domain interaction with the phospholipid PIP$_2$ in the AZ membrane, therefore disrupting the tight link between SVs and the release site (de Jong et al., 2018). Another key finding of our study is the delocalization of tightly docked SVs from the AZ c.o.m. in RIM1$\alpha^{-/-}$ (Figures 4A–4E). Regarding this observation, one may wonder about the molecular arrangement of release site defining AZ components such as Munc13-1 and VGCCs in RIM1$\alpha^{-/-}$. Interestingly, STED imaging in RIM-BP2 knockout mice revealed, that the distance of RIM and Cav2.1 increases up to 35% in MFBs (Brockmann et al., 2020). Electron tomographic analyses of NMJs in *Caenorhabditis elegans* have shown that in the absence of the RIM homologue *unc-10* SVs delocalize from dense projections, which define the center of the AZ, presumably due to a lost collaboration with *syd-2*, a homologue of the scaffold AZ protein α-Liprin (Stigloher et al., 2011).

EDM connecting SV and AZ membrane is altered in RIM1$\alpha^{-/-}$

We found EDM width reduced from 19.4 nm to 17.9 nm in tightly docked SVs in RIM1$\alpha^{-/-}$ AZs (Figure 3E). EDM width of SVs at 2.1–5 nm was further reduced to 14 nm in both genotypes. These

findings may be related to recently described hexagonal Munc13-1 protein densities in cryo-EM (Grushin et al., 2022; Rothman et al., 2017). The authors described a model with three states of Munc13-1 oligomers: in state 1, Munc13-1 is in the upright configuration under captured SVs of unassembled SNAREs. The closed hexagonal cage of pre-primed SVs in state 2 has a reduced diameter. In state 3 of primed SVs with approximate half-zippered SNARE pins the diameter of the hexagon widens because of calcium influx and binding to Munc-13 C_2B domains. In general terms, the magnitude and direction of the EDM changes in our study are in accordance with this 3-state model. Furthermore, the smaller EDM width in RIM1$\alpha^{-/-}$ might derive from the reduced expression of Munc13-1 at AZs (Grushin et al., 2022; Schoch et al., 2002). An additional explanation might be the missing interaction of PIP$_2$ with the C_2B domain of RIM1α. Regarding SV size, we found a small but significant increase of the absolute SV diameter in RIM1$\alpha^{-/-}$ (Figure 3F). Interestingly, Imig et al. described a similar increase in SV diameter in Munc13-1/2 double knockout (Imig et al., 2014). However, the causal relation between the absence of Munc-13 or RIM1α and the enlargement of SVs remains unclear.

Organization of the SV pool up to 200 nm is changed in RIM1$\alpha^{-/-}$

Consistent with previous findings (Fernandez-Busnadiego et al., 2013; Schoch et al., 2002), we report a reduced SV pool in proximity to the AZ membrane (0–50 nm, ~1 SV diameter plus SV protein coverage zone) for RIM1$\alpha^{-/-}$. In addition, our study shows an overall reduction of the total SV pool within 200 nm (~4 SV diameter) in the absence of RIM1α, suggesting two distinct "net"-works of neighboring SVs: a wider proximal pool (RRP) (Rizzoli and Betz, 2004; Rollenhagen and Lübke, 2010), and a denser cloud of SVs with increasing distance to the membrane without any differences in their NN configuration (recycling pool [Rollenhagen and Lübke, 2010]/reserve pool [Zhang and Augustine, 2021]) (Rizzoli and Betz, 2004; Rollenhagen and Lübke, 2010). Our differentiation is based on a 3D investigation of NN distances. Further theories involving RIM, RIM-BP, and VGCCs support the structural differentiation of the SV pool in functionally distinct parts (Milovanovic et al., 2018; Wu et al., 2019). Studies in conditional RIM/ELKS and ELKS1α/2α mice suggest that the interplay of both scaffold proteins is essential for presynaptic AZ composition, including the SV pool size and that in particular ELKS control the size of the RRP through its N-terminal coiled-coil domains (Held et al., 2016; Wang et al., 2016). We found a more heterogeneous distribution of SVs within the SV pool up to 200 nm resulting in overall decreased SV density per area, however (and somehow counterintuitive) also decreased NN1-5 distances in RIM1$\alpha^{-/-}$ (Figures 4G and 4H). We believe this can be interpreted as accumulation of SVs in "nests" in RIM1$\alpha^{-/-}$ compared with a more homogenous SV distribution in wild-type AZs. Although, the molecular mechanism of this "nest" formation remains unclear, one might speculate that it relates to synapsins and their role in SV reserve pools (Owe et al., 2009; Zhang and Augustine, 2021).

We find an increased accumulation of mitochondria in RIM1$\alpha^{-/-}$ AZs (Figure S2). The expansion of AZ surface area, synaptic cleft, and delocalization of docked SVs in RIM1$\alpha^{-/-}$

might raise energy consumption (Devine and Kittler, 2018; Pulido and Ryan, 2021). Greater proximity of mitochondria and AZs should facilitate calcium and ATP supply for the SV pool and the AZ membrane.

Limitations of the study

Using EM tomography on near-to-natively prepared 250-nm semithin sections of giant MFB AZs for quantification has unavoidable limitations. Acute slice preparation, immediate cryo-immobilization and freeze substitution can influence sample quality, e.g., potential tissue alteration by cryoprotectants (PVP) although no alteration was reported (Borges-Merjane et al., 2020), or by prolonged preparation processes (Bischofberger et al., 2006), air bubbles during high-pressure freezing and the time-consuming freeze substitution (7 days). Although our present method yielded high-quality EM tomograms in nanometer resolution, 3D mapping of entire giant MFB AZs is limited by their complex structure (Rollenhagen et al., 2007; Wilke et al., 2013) and would require advanced EM tomography techniques (e.g., STEM tomography with thicker tissue sections). For large-scale quantification of AZs on entire spiny excrescences, different volume EM techniques (e.g., SBF-SEM, FIB-SEM) are available (Wilke et al., 2013); however, with an obvious lack of the needed ultrastructural resolution for the precise 3D analysis of individual SVs.

Our study focused on characterization of AZ ultrastructure and SV pool arrangement in a distinct giant MFB-to-CA3b pyramidal cell synapse in RIM1$\alpha^{-/-}$ and wild-type mice. Functional characterization of MFBs was not performed in the present study. As deficiency of RIM1α impairs long-term potentiation (LTP) (Castillo et al., 2002) and associative and spatial learning (Powell et al., 2004) but not short-term plasticity or baseline synaptic transmission in giant MFB synapses (Castillo et al., 2002), it is remarkable that ultrastructure of RIM1$\alpha^{-/-}$ giant MFB AZs is altered. It raises the question of which direct or indirect ultrastructural changes in RIM1$\alpha^{-/-}$ AZs compensate baseline activity, and which might lead to impaired LTP. Without further functional characterization and EM tomographic studies of giant MFBs after LTP induction, this remains speculative. Even if SV pool reorganization and delocalization in RIM1$\alpha^{-/-}$ mice could be argued to most likely affect plasticity, the previously reported functional characterization of MFBs using measurements of field potentials in mossy fiber tract (Castillo et al., 2002) might have lacked the resolution to directly relate function to ultrastructural changes in individual MFB AZs. Our present characterization of MFB ultrastructure could serve as a basis for future studies using more advanced electrophysiological methods, such as paired patch-clamp recordings to relate changes in ultrastructure to basic synaptic transmission and MFB plasticity.

STAR★METHODS

Detailed methods are provided in the online version of this paper and include the following:

- KEY RESOURCES TABLE
- RESOURCE AVAILABILITY
  - Lead contact
  - Materials availability
  - Data and code availability
- EXPERIMENTAL MODEL AND SUBJECT DETAILS
  - Mouse line
- METHOD DETAILS
  - General
  - Slice preparation
  - Cryo-immobilization of acute brain slices
  - Freeze substitution
  - Flat embedding
  - Sample processing
  - Electron tomography
  - Selection of samples and region of interest
  - Image analysis and tomogram segmentation
  - 2D and 3D quantitative data evaluation
- QUANTIFICATION AND STATISTICAL ANALYSIS
  - Data availability

SUPPLEMENTAL INFORMATION

Supplemental information can be found online at https://doi.org/10.1016/j.celrep.2022.111382.

AUTHOR CONTRIBUTIONS

Conceptualization: K.L., C.S., M.H., and A.-L.S.; *Methodology*: K.L., C.S., M.H., and A.-L.S.; K.L. and M.P. established rapid cryo-immobilization of acute brain slices. S.S. provided the mouse line. *Investigation*: K.L. and C.S.; *Formal analysis*: K.L. under supervision of P.K., C.S., M.H., and A.-L.S.; *Validation, data interpretation*: K.L., M.M.P., C.S., M.H., and A.-L.S.; *Software*: K.L. and P.K.; *Resources*: C.S., M.H., and A.-L.S.; *Funding acquisition*: M.M.P., C.S., M.H., and A.-L.S.; *Data curation*: K.L., M.M.P., M.P., C.S., M.H., and A.-L.S.; *Writing - original draft*: K.L., M.M.P., M.H., and A-L.S.; *Writing - review & editing*: All authors. All authors read and approved the final manuscript.

DECLARATION OF INTERESTS

The authors declare no competing interests.

REFERENCES

Amaral, D.G., and Dent, J.A. (1981). Development of the mossy fibers of the dentate gyrus: I. A light and electron microscopic study of the mossy fibers and their expansions. J. Comp. Neurol. *195*, 51–86.

Andrews-Zwilling, Y.S., Kawabe, H., Reim, K., Varoqueaux, F., and Brose, N. (2006). Binding to Rab3A-interacting molecule RIM regulates the presynaptic recruitment of Munc13-1 and ubMunc13-2. J. Biol. Chem. *281*, 19720–19731.

Bischofberger, J., Engel, D., Li, L., Geiger, J.R.P., and Jonas, P. (2006). Patch-clamp recording from mossy fiber terminals in hippocampal slices. Nat. Protoc. *1*, 2075–2081.

Borges-Merjane, C., Kim, O., and Jonas, P. (2020). Functional electron microscopy, "flash and freeze, " of identified cortical synapses in acute brain slices. Neuron *108*, 992–1006.e6.

Brockhaus, J., Schreitmuller, M., Repetto, D., Klatt, O., Reissner, C., Elmslie, K., Heine, M., and Missler, M. (2018). alpha-Neurexins Together with alpha2-delta-1 Auxiliary Subunits Regulate Ca(2+) Influx through Cav2.1 Channels. The Journal of neuroscience : the official journal of the Society for Neuroscience *38*, 8277–8294. https://doi.org/10.1523/JNEUROSCI.0511-18.2018.

Brockmann, M.M., Zarebidaki, F., Camacho, M., Grauel, M.K., Trimbuch, T., Südhof, T.C., and Rosenmund, C. (2020). A trio of active zone proteins comprised of RIM-BPs, RIMs, and Munc13s governs neurotransmitter release. Cell Rep. *32*, 107960.

Butola, T., Alvanos, T., Hintze, A., Koppensteiner, P., Kleindienst, D., Shigemoto, R., Wichmann, C., and Moser, T. (2021). RIM-binding protein 2 organizes Ca(2+) channel topography and regulates release probability and vesicle replenishment at a fast central synapse. J. Neurosci. *41*, 7742–7767.

Camacho, M., Basu, J., Trimbuch, T., Chang, S., Pulido-Lozano, C., Chang, S.S., Duluvova, I., Abo-Rady, M., Rizo, J., and Rosenmund, C. (2017). Heterodimerization of Munc13 C2A domain with RIM regulates synaptic vesicle docking and priming. Nat. Commun. *8*, 15293.

Castillo, P.E., Schoch, S., Schmitz, F., Südhof, T.C., and Malenka, R.C. (2002). RIM1alpha is required for presynaptic long-term potentiation. Nature *415*, 327–330.

de Jong, A.P.H., Roggero, C.M., Ho, M.R., Wong, M.Y., Brautigam, C.A., Rizo, J., and Kaeser, P.S. (2018). RIM C2B domains target presynaptic active zone functions to PIP2-containing membranes. Neuron *98*, 335–349.e7.

Deng, L., Kaeser, P.S., Xu, W., and Südhof, T.C. (2011). RIM proteins activate vesicle priming by reversing autoinhibitory homodimerization of Munc13. Neuron *69*, 317–331.

Devine, M.J., and Kittler, J.T. (2018). Mitochondria at the neuronal presynapse in health and disease. Nat. Rev. Neurosci. *19*, 63–80.

Emperador-Melero, J., and Kaeser, P.S. (2020). Assembly of the presynaptic active zone. Curr. Opin. Neurobiol. *63*, 95–103.

Fernandez-Busnadiego, R., Asano, S., Oprisoreanu, A.M., Sakata, E., Doengi, M., Kochovski, Z., Zurner, M., Stein, V., Schoch, S., Baumeister, W., et al. (2013). Cryo-electron tomography reveals a critical role of RIM1alpha in synaptic vesicle tethering. J. Cell Biol. *201*, 725–740.

Galimberti, I., Gogolla, N., Alberi, S., Santos, A.F., Muller, D., and Caroni, P. (2006). Long-term rearrangements of hippocampal mossy fiber terminal connectivity in the adult regulated by experience. Neuron *50*, 749–763.

Gillies, S., Bierbaum, A., Lautaportti, K., and Tonnhofer, O. (2007). Shapely: manipulation and analysis of geometric objects. https://github.com/Toblerity/Shapely.

Goodsell, D.S., Olson, A.J., and Forli, S. (2020). Art and science of the cellular mesoscale. Trends Biochem. Sci. *45*, 472–483.

Gray, E.G. (1959). Electron microscopy of synaptic contacts on dendrite spines of the cerebral cortex. Nature *183*, 1592–1593.

Grushin, K., Kalyana Sundaram, R.V., Sindelar, C.V., and Rothman, J.E. (2022). Munc13 structural transitions and oligomers that may choreograph successive stages in vesicle priming for neurotransmitter release. Proc. Natl. Acad. Sci. USA *119*, e2121259119.

Hacker, C., and Lucocq, J.M. (2014). Analysis of specificity in immunoelectron microscopy. Methods Mol. Biol. *1117*, 315–323.

Hallermann, S., Pawlu, C., Jonas, P., and Heckmann, M. (2003). A large pool of releasable vesicles in a cortical glutamatergic synapse. Proc. Natl. Acad. Sci. USA *100*, 8975–8980.

Han, Y., Kaeser, P.S., Südhof, T.C., and Schneggenburger, R. (2011). RIM determines Ca(2)+ channel density and vesicle docking at the presynaptic active zone. Neuron *69*, 304–316.

Harlow, M.L., Ress, D., Stoschek, A., Marshall, R.M., and McMahan, U.J. (2001). The architecture of active zone material at the frog's neuromuscular junction. Nature *409*, 479–484.

Harris, C.R., Millman, K.J., van der Walt, S.J., Gommers, R., Virtanen, P., Cournapeau, D., Wieser, E., Taylor, J., Berg, S., Smith, N.J., et al. (2020). Array programming with NumPy. Nature *585*, 357–362.

Held, R.G., Liu, C., and Kaeser, P.S. (2016). ELKS controls the pool of readily releasable vesicles at excitatory synapses through its N-terminal coiled-coil domains. Elife *5*, e14862.

Henze, D.A., Wittner, L., and Buzsáki, G. (2002). Single granule cells reliably discharge targets in the hippocampal CA3 network in vivo. Nat. Neurosci. *5*, 790–795.

Hibino, H., Pironkova, R., Onwumere, O., Vologodskaia, M., Hudspeth, A.J., and Lesage, F. (2002). RIM binding proteins (RBPs) couple Rab3-interacting molecules (RIMs) to voltage-gated Ca(2+) channels. Neuron *34*, 411–423.

Imig, C., López-Murcia, F.J., Maus, L., García-Plaza, I.H., Mortensen, L.S., Schwark, M., Schwarze, V., Angibaud, J., Nägerl, U.V., Taschenberger, H., et al. (2020). Ultrastructural imaging of activity-dependent synaptic membrane-trafficking events in cultured brain slices. Neuron *108*, 843–860.e8.

Imig, C., Min, S.W., Krinner, S., Arancillo, M., Rosenmund, C., Südhof, T.C., Rhee, J., Brose, N., and Cooper, B.H. (2014). The morphological and molecular nature of synaptic vesicle priming at presynaptic active zones. Neuron *84*, 416–431.

Jonas, P., Major, G., and Sakmann, B. (1993). Quantal components of unitary EPSCs at the mossy fibre synapse on CA3 pyramidal cells of rat hippocampus. J. Physiol. *472*, 615–663.

Kaeser, P.S., Deng, L., Fan, M., and Südhof, T.C. (2012). RIM genes differentially contribute to organizing presynaptic release sites. Proc. Natl. Acad. Sci. USA *109*, 11830–11835.

Kaeser, P.S., Deng, L., Wang, Y., Dulubova, I., Liu, X., Rizo, J., and Südhof, T.C. (2011). RIM proteins tether Ca2+ channels to presynaptic active zones via a direct PDZ-domain interaction. Cell *144*, 282–295.

Kaeser, P.S., and Regehr, W.G. (2017). The readily releasable pool of synaptic vesicles. Curr. Opin. Neurobiol. *43*, 63–70.

Kheirbek, M.A., Drew, L.J., Burghardt, N.S., Costantini, D.O., Tannenholz, L., Ahmari, S.E., Zeng, H., Fenton, A.A., and Hen, R. (2013). Differential control of learning and anxiety along the dorsoventral axis of the dentate gyrus. Neuron *77*, 955–968.

Kintscher, M., Wozny, C., Johenning, F.W., Schmitz, D., and Breustedt, J. (2013). Role of RIM1alpha in short- and long-term synaptic plasticity at cerebellar parallel fibres. Nat. Commun. *4*, 2392.

Kiyonaka, S., Wakamori, M., Miki, T., Uriu, Y., Nonaka, M., Bito, H., Beedle, A.M., Mori, E., Hara, Y., De Waard, M., et al. (2007). RIM1 confers sustained activity and neurotransmitter vesicle anchoring to presynaptic Ca2+ channels. Nat. Neurosci. *10*, 691–701.

Kluyver, T., Ragan-Kelley, B., Pérez, F., Granger, B., Bussonnier, M., Frederic, J., Kelley, K., Hamrick, J., Grout, J., Corlay, S., et al. (2016). Jupyter Notebooks – a Publishing Format for Reproducible Computational Workflows (IOS Press - Positioning and Power in Academic Publishing: Players, Agents and Agendas), pp. 87–90.

Korogod, N., Petersen, C.C., and Knott, G.W. (2015). Ultrastructural analysis of adult mouse neocortex comparing aldehyde perfusion with cryo fixation. Elife *4*, e05793.

Kremer, J.R., Mastronarde, D.N., and McIntosh, J.R. (1996). Computer visualization of three-dimensional image data using IMOD. J. Struct. Biol. *116*, 71–76.

Kusick, G.F., Chin, M., Raychaudhuri, S., Lippmann, K., Adula, K.P., Hujber, E.J., Vu, T., Davis, M.W., Jorgensen, E.M., and Watanabe, S. (2020). Synaptic vesicles transiently dock to refill release sites. Nat. Neurosci. *23*, 1329–1338.

Lawrence, J.J., Grinspan, Z.M., and McBain, C.J. (2004). Quantal transmission at mossy fibre targets in the CA3 region of the rat hippocampus. J. Physiol. *554*, 175–193.

Markert, S.M., Skoruppa, M., Yu, B., Mulcahy, B., Zhen, M., Gao, S., Sendtner, M., and Stigloher, C. (2020). Overexpression of an ALS-associated FUS mutation in C. elegans disrupts NMJ morphology and leads to defective neuromuscular transmission. Biol. Open 9, bio055129.

Martinez-Sanchez, A., Laugks, U., Kochovski, Z., Papantoniou, C., Zinzula, L., Baumeister, W., and Lucic, V. (2021). Trans-synaptic assemblies link synaptic vesicles and neuroreceptors. Sci Adv 7, eabe6204. https://doi.org/10.1126/sciadv.abe6204.

Mastronarde, D.N. (2005). Automated electron microscope tomography using robust prediction of specimen movements. J. Struct. Biol. 152, 36–51.

Masukawa, L.M., Benardo, L.S., and Prince, D.A. (1982). Variations in electrophysiological properties of hippocampal neurons in different subfields. Brain Res. 242, 341–344.

Maus, L., Lee, C., Altas, B., Sertel, S.M., Weyand, K., Rizzoli, S.O., Rhee, J., Brose, N., Imig, C., and Cooper, B.H. (2020). Ultrastructural correlates of presynaptic functional heterogeneity in hippocampal synapses. Cell Rep. 30, 3632–3643.e8.

Miki, T., Kiyonaka, S., Uriu, Y., De Waard, M., Wakamori, M., Beedle, A.M., Campbell, K.P., and Mori, Y. (2007). Mutation associated with an autosomal dominant cone-rod dystrophy CORD7 modifies RIM1-mediated modulation of voltage-dependent Ca2+ channels. Channels 1, 144–147.

Milovanovic, D., Wu, Y., Bian, X., and De Camilli, P. (2018). A liquid phase of synapsin and lipid vesicles. Science 361, 604–607.

Mrestani, A., Pauli, M., Kollmannsberger, P., Repp, F., Kittel, R.J., Eilers, J., Doose, S., Sauer, M., Sirén, A.L., Heckmann, M., and Paul, M.M. (2021). Active zone compaction correlates with presynaptic homeostatic potentiation. Cell Rep. 37, 109770.

Müller, M., Liu, K.S.Y., Sigrist, S.J., and Davis, G.W. (2012). RIM controls homeostatic plasticity through modulation of the readily-releasable vesicle pool. J. Neurosci. 32, 16574–16585.

Neher, E., and Brose, N. (2018). Dynamically primed synaptic vesicle states: key to understand synaptic short-term plasticity. Neuron 100, 1283–1291.

Orlando, M., Dvorzhak, A., Bruentgens, F., Maglione, M., Rost, B.R., Sigrist, S.J., Breustedt, J., and Schmitz, D. (2021). Recruitment of release sites underlies chemical presynaptic potentiation at hippocampal mossy fiber boutons. PLoS Biol. 19, e3001149.

Owe, S.G., Jensen, V., Evergren, E., Ruiz, A., Shupliakov, O., Kullmann, D.M., Storm-Mathisen, J., Walaas, S.I., Hvalby, Ø., and Bergersen, L.H. (2009). Synapsin- and actin-dependent frequency enhancement in mouse hippocampal mossy fiber synapses. Cerebr. Cortex 19, 511–523.

Paul, M.M., Dannhäuser, S., Morris, L., Mrestani, A., Hübsch, M., Gehring, J., Hatzopoulos, G.N., Pauli, M., Auger, G.M., Bornschein, G., et al. (2022). The human cognition-enhancing CORD7 mutation increases active zone number and synaptic release. Brainawac011.

Pauli, M., Paul, M.M., Proppert, S., Mrestani, A., Sharifi, M., Repp, F., Kürzinger, L., Kollmannsberger, P., Sauer, M., Heckmann, M., and Sirén, A.L. (2021). Targeted volumetric single-molecule localization microscopy of defined presynaptic structures in brain sections. Commun. Biol. 4, 407.

Pedregosa, F., Varoquaux, G., Gramfort, A., Michel, V., Thirion, B., Grisel, O., Blondel, M., Prettenhofer, P., Weiss, R., Dubourg, V., et al. (2011). Scikit-learn: machine learning in Python. J. Mach. Learn. Res. 12, 2825–2830.

Powell, C.M., Schoch, S., Monteggia, L., Barrot, M., Matos, M.F., Feldmann, N., Südhof, T.C., and Nestler, E.J. (2004). The presynaptic active zone protein RIM1alpha is critical for normal learning and memory. Neuron 42, 143–153.

Pulido, C., and Ryan, T.A. (2021). Synaptic vesicle pools are a major hidden resting metabolic burden of nerve terminals. Sci. Adv. 7, eabi9027.

Reynolds, E.S. (1963). The use of lead citrate at high pH as an electron-opaque stain in electron microscopy. J. Cell Biol. 17, 208–212.

Rizzoli, S.O., and Betz, W.J. (2004). The structural organization of the readily releasable pool of synaptic vesicles. Science 303, 2037–2039.

Rollenhagen, A., and Lübke, J.H.R. (2010). The mossy fiber bouton: the "common" or the "unique" synapse? Front. Synaptic Neurosci. 2, 2.

Rollenhagen, A., Sätzler, K., Rodríguez, E.P., Jonas, P., Frotscher, M., and Lübke, J.H.R. (2007). Structural determinants of transmission at large hippocampal mossy fiber synapses. J. Neurosci. 27, 10434–10444.

Rostaing, P., Real, E., Siksou, L., Lechaire, J.P., Boudier, T., Boeckers, T.M., Gertler, F., Gundelfinger, E.D., Triller, A., and Marty, S. (2006). Analysis of synaptic ultrastructure without fixative using high-pressure freezing and tomography. Eur. J. Neurosci. 24, 3463–3474.

Rothman, J.E., Krishnakumar, S.S., Grushin, K., and Pincet, F. (2017). Hypothesis - buttressed rings assemble, clamp, and release SNAREpins for synaptic transmission. FEBS Lett. 591, 3459–3480.

Savtchenko, L.P., and Rusakov, D.A. (2007). The optimal height of the synaptic cleft. Proc Natl Acad Sci U S A 104, 1823–1828. https://doi.org/10.1073/pnas.0606636104.

Schindelin, J., Arganda-Carreras, I., Frise, E., Kaynig, V., Longair, M., Pietzsch, T., Preibisch, S., Rueden, C., Saalfeld, S., Schmid, B., et al. (2012). Fiji: an open-source platform for biological-image analysis. Nat. Methods 9, 676–682.

Schoch, S., Castillo, P.E., Jo, T., Mukherjee, K., Geppert, M., Wang, Y., Schmitz, F., Malenka, R.C., and Südhof, T.C. (2002). RIM1alpha forms a protein scaffold for regulating neurotransmitter release at the active zone. Nature 415, 321–326.

Schoch, S., Mittelstaedt, T., Kaeser, P.S., Padgett, D., Feldmann, N., Chevaleyre, V., Castillo, P.E., Hammer, R.E., Han, W., Schmitz, F., et al. (2006). Redundant functions of RIM1alpha and RIM2alpha in Ca(2+)-triggered neurotransmitter release. EMBO J. 25, 5852–5863.

Seabold, S., and Perktold, J. (2010). Statsmodels: econometric and statistical modeling with Python. In Paper Presented at: SkyPy 2010 (Austin, Texas).

Siksou, L., Rostaing, P., Lechaire, J.P., Boudier, T., Ohtsuka, T., Fejtová, A., Kao, H.T., Greengard, P., Gundelfinger, E.D., Triller, A., and Marty, S. (2007). Three-dimensional architecture of presynaptic terminal cytomatrix. J. Neurosci. 27, 6868–6877.

Stigloher, C., Zhan, H., Zhen, M., Richmond, J., and Bessereau, J.L. (2011). The presynaptic dense projection of the Caenorhabditis elegans cholinergic neuromuscular junction localizes synaptic vesicles at the active zone through SYD-2/liprin and UNC-10/RIM-dependent interactions. J. Neurosci. 31, 4388–4396.

Tang, A.H., Chen, H., Li, T.P., Metzbower, S.R., MacGillavry, H.D., and Blanpied, T.A. (2016). A trans-synaptic nanocolumn aligns neurotransmitter release to receptors. Nature 536, 210–214.

van Rossum, G., and de Boer, J. (1991). Linking a stub generator (AIL) to a prototyping language (Python). In Paper Presented at: EurOpen Conference Proceedings (May 20-24, 1991) (Tromso, Norway).

Vyleta, N.P., and Jonas, P. (2014). Loose coupling between Ca2+ channels and release sensors at a plastic hippocampal synapse. Science 343, 665–670.

Wang, S.S.H., Held, R.G., Wong, M.Y., Liu, C., Karakhanyan, A., and Kaeser, P.S. (2016). Fusion competent synaptic vesicles persist upon active zone disruption and loss of vesicle docking. Neuron 91, 777–791.

Wang, Y., Liu, X., Biederer, T., and Südhof, T.C. (2002). A family of RIM-binding proteins regulated by alternative splicing: implications for the genesis of synaptic active zones. Proc. Natl. Acad. Sci. USA 99, 14464–14469.

Wang, Y., Okamoto, M., Schmitz, F., Hofmann, K., and Südhof, T.C. (1997). Rim is a putative Rab3 effector in regulating synaptic-vesicle fusion. Nature 388, 593–598.

Weimer, R.M. (2006). Preservation of C. elegans tissue via high-pressure freezing and freeze-substitution for ultrastructural analysis and immunocytochemistry. Methods Mol. Biol. 351, 203–221.

Wilke, S.A., Antonios, J.K., Bushong, E.A., Badkoobehi, A., Malek, E., Hwang, M., Terada, M., Ellisman, M.H., and Ghosh, A. (2013). Deconstructing complexity: serial block-face electron microscopic analysis of the hippocampal mossy fiber synapse. J. Neurosci. 33, 507–522.

Wu, X., Cai, Q., Shen, Z., Chen, X., Zeng, M., Du, S., and Zhang, M. (2019). RIM and RIM-BP form presynaptic active-zone-like condensates via phase separation. Mol. Cell *73*, 971–984.e5.

Zarebidaki, F., Camacho, M., Brockmann, M.M., Trimbuch, T., Herman, M.A., and Rosenmund, C. (2020). Disentangling the roles of RIM and Munc13 in synaptic vesicle localization and neurotransmission. J. Neurosci. *40*, 9372–9385.

Zhang, M., and Augustine, G.J. (2021). Synapsins and the synaptic vesicle reserve pool: floats or anchors? Cells *10*, 658.

Zhao, S., Studer, D., Chai, X., Graber, W., Brose, N., Nestel, S., Young, C., Rodriguez, E.P., Saetzler, K., and Frotscher, M. (2012). Structural plasticity of hippocampal mossy fiber synapses as revealed by high-pressure freezing. J. Comp. Neurol. *520*, 2340–2351.

STAR★METHODS

KEY RESOURCES TABLE

REAGENT or RESOURCE	SOURCE	IDENTIFIER
Chemicals, peptides, and recombinant proteins		
Acetone dry (max. 0.01% water)	AppliChem	481007; CAS: 67-64-1
Calcium chloride	Sigma-Aldrich	223506; CAS: 10035-04-8
Dodecenylsuccinic anhydride (DDSA)	Serva	20755.02; CAS: 26544-38-7
Ethanol absolute	Chemsolute	2246.2500, CAS: 64-17-5
Glucose	Sigma-Aldrich	G7021; CAS: 50-99-7
10 % Glutaraldehyde (anhydrous, EM grade) in acetone	Electron Microscopy Sciences	16530; CAS: N/A
25 % Glutaraldehyde (aqueous solution)	Electron Microscopy Sciences	16220, CAS: N/A
Glycid ether 100	Serva Electrophoresis GmbH	21045.02, CAS: 90529-77-4
Isoflurane (1 mL/mL)	CP-Pharma	Y0000858
Magnesium chloride	Sigma-Aldrich	M9272; CAS: 7791-18-6
Methylnadic anhydride (MNA)	Serva Electrophoresis GmbH	29452.01; CAS: 25134-21-8
Osmium Tetroxide	Science Services	E19110, CAS: 20816-12-0
Pioloform (polyvinyl butyral)	Plano	R1275, CAS: 63148-64-1
Polyvinylpyrrolidone (PVP)	Sigma-Aldrich	PVP40; CAS: 9003-39-8
Potassium chloride	Sigma-Aldrich	P9333, CAS: 7447-40-7
Sodium bicarbonate	Sigma-Aldrich	S5761; CAS: 144-55-8
Sodium chloride	Sigma-Aldrich	S7653; CAS: 7647-14-5
Sodium hydroxide pellets	Sigma-Aldrich	1.06482, CAS: 1310-73-2
Sodium phosphate	Aldon CORP SE	SS0756-500GR; CAS: 7558-80-7
Sucrose	Sigma-Aldrich	S0389; CAS: 57-50-1
SYLGARD® 184	Sigma-Aldrich	761036; CAS: N/A
Tannic acid	AppliChem	141065, CAS: 1401-55-4
2,4,6-Tris(dimethylaminomethyl)phenol (DMP-30)	Serva Electrophoresis GmbH	26975.03, CAS: 90-72-2
Uranyl Acetate	Science Services	E22400, CAS: 6159-44-0 (541-09-3)
Experimental models: Organisms/strains		
Mus musculus: B6;129P2-Rims1[tm1SudJ]	Breeders provided by Susanne Schoch, (Schoch et al., 2002)	N/A
Software and algorithms		
Adobe Illustrator (2021)	Adobe	RRID: SCR_010279; http://www.adobe.com/products/illustrator.html
Allen Reference Atlas - Mouse Brain (Adult, 3D coronal)	Allen Brain Institute	RRID: SCR_013286; http://mouse.brain-map.org/static/atlas
EM-MENU 4.0	Tietz Video and Image Processing Systems	https://www.tvips.com/imaging-software/em-menu/
Fiji (v1.53 n)	(Schindelin et al., 2012)	RRID: SCR_002285; http://fiji.sc
IMOD	(Kremer et al., 1996)	RRID: SCR_003297; http://bio3d.colorado.edu/imod
Jupyter Notebook	(Kluyver et al., 2016)	RRID: SCR_018315; https://jupyter.org/
NumPy	(Harris et al., 2020)	RRID: SCR_008633; http://www.numpy.org
OriginPro (2021)	Origin Lab	RRID: SCR_014212; http://www.originlab.com/index.aspx?go=PRODUCTS/Origin
scikit-learn	(Pedregosa et al., 2011)	RRID: SCR_002577; http://scikit-learn.org/

Continued

REAGENT or RESOURCE	SOURCE	IDENTIFIER
SerialEM	(Mastronarde, 2005)	RRID: SCR_017293; http://bio3d.colorado.edu/SerialEM/
Shapely	(Gillies et al., 2007)	N/A
Custom-written Python code	This paper	https://zenodo.org/record/6952807
SigmaPlot 14	Systat Software	RRID: SCR_003210; http://www.sigmaplot.com/products/sigmaplot/
Statsmodels	(Seabold and Perktold, 2010)	RRID: SCR_016074; http://www.statsmodels.org/
Other		
Leica EM HPM100 freezer	Leica Microsystems	RRID: SCR_021366; https://www.leica-microsystems.com/de/produkte/em-probenvorbereitung/p/leica-em-hpm100/
Leica EM AFS2 freeze substitution device	Leica Microsystems	RRID: SCR_020230; https://www.leica-microsystems.com/products/sample-preparation-for-electron-microscopy/p/leica-em-afs2/
Leica EM UC7 ultramicrotome	Leica Microsystems	RRID: SCR_016694; https://www.leica-microsystems.com/de/produkte/em-probenvorbereitung/ultramikrotome-kryo-ultramikrotome/details/product/leica-em-uc7/
Leica VT1200 S vibrating microtome	Leica Microsystems	RRID: SCR_020243; https://www.leicabiosystems.com/histology-equipment/sliding-and-vibrating-blade-microtomes/vibrating-blade-microtomes/leica-vt1200-s/
TemCam F416 4kx4k	Tietz Video and Image Processing Systems	RRID: N/A; https://www.tvips.com/camera-systems/temcam-f-series/
CCU-010 HV compact coating unit	Safematic	RRID: N/A; https://www.safematic.ch/ccu-010-hv-sputter-coater-vacuum-coating-system-switzerland.php
ACLAR® embedding film	Ted Pella	10501
TEM single slot grid (copper)	Plano	G2500C
TEM 50 mesh grid (copper)	Plano	G2050C
Carrier, 3 mm, 200 μm, type A	Baltic Präparation	BP2135-3
Carrier, 3 mm, 300 μm, type B	Baltic Präparation	BP2136-3

RESOURCE AVAILABILITY

Lead contact
Further information and requests for resources and reagents should be directed to and will be fulfilled by the lead contact, Anna-Leena Sirén (anna-leena.siren@uni-wuerzburg.de).

Materials availability
This study did not generate new unique reagents.

Data and code availability

- All datasets supporting the findings of this work will be shared by the lead contact upon request. The original code has been deposited at GitHub and is publicly available as of the date of publication, DOI is listed in the Key resources table.
- Any additional information required to reanalyze the data reported in this paper is available from the lead contact upon request.

EXPERIMENTAL MODEL AND SUBJECT DETAILS

Mouse line

The mouse line (B6; 129P2-Rims1^tm1Sud/J, Schoch et al., 2002) was provided by Susanne Schoch. Three male RIM1α knock-out mice (RIM1α$^{-/-}$) and three male wild-type littermates (RIM1α$^{+/+}$) at an age of 13–19 weeks were used for the experimental procedure. Animal breeding, animal housing and all experimental procedures were carried out in accordance with the German regulations and guidelines for animal experimentation, the EU Directive 2010/63/EU as well as the United States Public Health Service's Policy on Humane Care and Use of Laboratory Animals and approved by the district government of Lower Franconia in Germany as the responsible authority (Permit Number RUF-55.2.2.-2532-2-571-11).

METHOD DETAILS

General

All procedures from preparation and cryo-immobilization of acute brain slices to selection of synaptic contacts and image analysis were performed by an investigator blinded to the genotype.

Slice preparation

Acute brain slices were prepared as described previously for patch-clamp recordings of hippocampal mossy fiber synapses (Bischofberger et al., 2006), with modifications. In brief, mice were anesthetized with isoflurane (1 mL/mL, CP-Pharma) and decapitated in deep anesthesia with a pair of scissors at the level of the cervical medulla. The head was dropped into ice-cold artificial cerebrospinal fluid (ACSF, containing 125 mM NaCl, 25 mM NaHCO$_3$, 2.5 mM KCl, 1.25 mM NaH$_2$PO$_4$, 25 mM glucose, 2 mM CaCl$_2$ and 1 mM MgCl$_2$, equilibrated with 95% O$_2$/5% CO$_2$, pH 7.3). The skin surrounding the head was removed carefully, then the skull cap was opened with a single sagittal cut from the foramen magnum to the olfactory bulb. Right and left part of the skull cap were separated without any contact to the ventral side of the brain. Two coronal cuts were made at the level of cerebellum and olfactory bulb to separate the entire brain from its skull basis using a small spatula. Due to possible time sensitive changes of cellular brain morphology (Bischofberger et al., 2006), the procedure was kept at a maximum preparation time of 60–90 s. With its ventral surface, the brain was mounted on a cutting chamber, containing a high sucrose cutting solution (ACSF, supplemented with 75 mM sucrose), of a Leica VT1200 vibratome (Leica Microsystems). Four consecutive horizontal sections of 200 μm thickness were cut at a defined level of the dorsal hippocampus. This region was defined by the Allan Mouse Brain Atlas (Version: Mouse, Adult, 3D coronal) approximately 2600 μm below the dorsal brain surface) and beginning from the first clear appearance of both dentate gyrus (DG) and *cornu ammonis* (CA).

Cryo-immobilization of acute brain slices

Cryo-immobilization of acute brain slices was performed using a slightly modified protocol for morphological analysis of synaptic contacts in *C. elegans* and *M. musculus* (Borges-Merjane et al., 2020; Markert et al., 2020; Stigloher et al., 2011). In brief, brain slices were transferred onto pre-cooled petri dishes coated with a silicone elastomer (Sylgard 184, Sigma-Aldrich) containing ice-cold ACSF. Slices were cut down to the left, entirely intact hippocampal region using a fine scalpel and loaded into high pressure freezing carriers (type A, 3 mm diameter and 200 μm depth, Baltic Präparation). The bottom carrier was overfilled slightly with precooled 15% polyvinyl-pyrrolidone in ice-cold ACSF, so that the liquid formed a convex hull upon the carrier itself. To avoid harming tissue integrity during manipulation, slices were enclosed into ACSF droplets for transfer. A second carrier (type B, 3 mm diameter and 300 μm depth, Baltic Präparation) was placed onto the first serving as a flat lid, taking advantage of the convex hull formed by ACSF to avoid a formation of air bubbles within the final carrier sandwich. Samples were processed at a freezing speed >20000 Ks^{-1} and a pressure >2100 bar with the high-pressure freezing machine EM HPM100 (Leica Microsystems).

Freeze substitution

High-pressure frozen brain samples were transferred separately into a single small plastic container of the EM AFS2 freeze substitution (FS) system (Leica Microsystems). High pressure freezing chamber sandwiches were opened to allow better penetration during freeze substitution. Samples were incubated as described previously (Markert et al., 2020; Stigloher et al., 2011). Briefly, samples were kept in anhydrous acetone containing 0.1% tannic acid and 0.5% glutaraldehyde for 20 h at −90°C. Then, the solution was replaced entirely by a fresh solution to avoid possible hydrous saturation of acetone caused by the initial sample loading of the AFS system. Samples were kept in the first FS solution for a total of 96 h at −90°C, followed by four washing steps with anhydrous acetone within 1 h. Thereafter, the samples were incubated in 2% OsO$_4$ in anhydrous acetone for 28 h at −90°C and heated slowly by an increase of temperature from −90°C to −20°C within 14 h. At −20°C, the pellets were incubated for 16 h. Then, the temperature was increased to 4°C in 4 h. After four washing steps (0.5 h interval) with anhydrous acetone, the temperature was increased to 20°C in 1 h. Subsequently, the samples were transferred in a freshly prepared epoxy resin solutions of 50% of the epoxy resin (EPON, component A: 50 mL Dodecenylsuccinic anhydride (DDSA), 31 mL glycid ether 100; component B: 44.5 mL methylnadic anhydride (MNA), 50 mL glycid ether 100; component C: 0.5 mL 2,4,6-Tris(dimethylaminomethyl)phenol (DMP-30); SERVA Electrophoresis GmbH) in acetone for 3 h at room temperature, 90% epoxy resin in acetone overnight at 4°C, and 3 times in 100% epoxy resin at

room temperature. During the infiltration process, the intact tissue pellets were solved carefully from the carrier to allow better epoxy resin penetration.

Flat embedding

Single tissue pellets, covered in 100% epoxy resin, were placed separately onto a sheet of transparent fluorinated-chlorinated thermoplastic (0.2 mm thickness, ACLAR®, Ted Pella). Thereafter, a second thermoplastic sheet was positioned as a lid upon the sample, thereby avoiding air bubbles between both sheets. The sandwich-like ensemble was weighted down by a small handmade aglet and masked at its sides to avoid a leakage of epoxy resin. The samples were polymerized for 48 h at 60°C.

Sample processing

The flat-embedded hippocampal slices were glued onto epoxy resin nibs without a thermoplastic sheet in between using cyanoacrylate. Tissue blocks were trimmed manually to trapezia containing the whole CA3 region and characteristic parts of the granule cell (GC) region for further orientation. Both ultrathin sections of 60–70 nm and semi-thin sections of 250 nm were cut with a Histo diamond knife (Diatome AG) at an EM UC7 ultramicrotome (Leica Microsystems). Ultrathin sections were positioned onto Pioloform (5% polyvinyl butyral in trichloromethane) coated copper grids (50 mesh, G2050C, Plano GmbH) to evaluate high pressure freezing quality of the tissue. 4–5 semi-thin hippocampal sections were positioned serially onto Pioloform coated, single slotted copper grids (2 × 1 mm, G2500C, Plano GmbH) for electron tomography. To prevent electron charging particularly at high tilt angles, single slot grids were coated by an approximately 3 nm thin layer of carbon using the high-vacuum carbon coating unit CCU-010 (Safematic GmbH). Both types of sections were contrasted with 5% uranyl acetate in ethanol for 7.5 min and 50% Reynolds' lead citrate (Reynolds, 1963) in $_{dd}H_2O$ for 10 min. In between both steps, the samples were washed in pure ethanol, in 50% ethanol in $_{dd}H_2O$ and pure $_{dd}H_2O$; after the contrasting, samples were washed three times in $_{dd}H_2O$ and blotted dry with filter paper.

Electron tomography

Both, electron micrographs and tilt image series of synapses were acquired at 200 kV using a JEM-2100 (JEOL) electron microscope equipped with a TemCam F416 4 k×4 k camera (Tietz Video and Image Processing Systems). Tilt series acquisition was carried out within a minimum range of −60° to +60° tilt angle with 1° increments at a pixel size of 0.287 nm. The SerialEM software package (Mastronarde, 2005) was used for image acquisition. To ensure an acquisition of presynaptic active zones (AZ) with an extraordinary AZ profile length the resolution had to be adjusted to 0.3897 nm per pixel at selected synapses during the experiments. For optimal acquisition conditions, a full electron beam alignment was conducted prior to each tilt series.

Selection of samples and region of interest

All HPF/FS, epoxy resin embedded brain slices were evaluated depending on possible freezing and/or embedding artefacts, i.e., formation of ice crystals (in particular, in the chromatin of cell nuclei, where they typically appear first), volumetric changes of cellular compartments and extracellular space. The appearance and intactness of lipid double layers, and the preservation of characteristic intracellular electron dense structures such as mitochondria and actin filaments were classified as criteria of high HPF/FS quality. Sample evaluation was carried in random order, coded by sample embedding number and not genotype. Only tissue slices which fulfilled the quality criteria for HPF/FS tissue (Weimer, 2006) were further processed for electron tomography. We observed that the quality of the HPF/FS brain sections declined depending on the time point of cutting at the vibratome. This may underpin a time sensitivity of the described protocol. Further, electron tomographic semi-thin sections were obtained within a minimum distance of 20–40 μm to the surface in slices with optimal tissue quality. If so, we could not observe any increased alteration of morphology due to possible cutting artefacts within 100 μm to the surface of the brain slice (Rostaing et al., 2006), or increasing formation of ice crystals with increasing distance to the center of the brain slice (Siksou et al., 2007). We collected tilt series at AZs of intact 2–5 μm giant mossy fiber boutons (Rollenhagen et al., 2007) alongside the left supra-pyramidal mossy fiber tract (*Stratum lucidum*) of the CA3b region (Masukawa et al., 1982). Postsynaptic spiny excrescences/spine heads of CA3b pyramidal neurons had to be clearly identifiable within the bouton, partially containing a spine apparatus (Gray, 1959) and PSF at the postsynaptic membrane opposite to AZ profiles. Giant MFB AZs were ultrastructurally defined as presynaptic compartments containing dense SVs clusters including docked SVs in near proximity to and at the presynaptic AZ membrane. The presynaptic 2D AZ profile and 3D AZ surface, respectively, were defined by their localization opposite to the postsynaptic membrane at which PSF were densely connected. Pre- and postsynaptic compartments were separated by the synaptic cleft, a characteristic widening between both membranes containing a network of electron-dense filaments. Membrane parts with and without PSFs were clearly distinguishable. Beside synaptic contacts at MF-CA3b pyramidal spine heads, all other synaptic contacts within the MFB were excluded from further analyses. To outweigh individual heterogeneity of MFB presynapses (Pauli et al., 2021; Wilke et al., 2013), we analyzed a minimum of 10 reconstructed tomograms per animal. Each reconstructed AZ tomogram consisted on average of 466 AZ profiles in RIM1α$^{+/+}$ and of 398 AZ profiles in RIM1α$^{-/-}$ mice (Figure 1F and Table S1). Only tomograms in which both pre- and postsynaptic membranes were clearly identifiable throughout the entire z stack were included into analysis.

Image analysis and tomogram segmentation

Tilt-image series alignment and tomographic reconstruction was performed with the ETomo/IMOD software package using a patch processing alignment and weighted back projection algorithm (Kremer et al., 1996). Overall, we observed a better alignment of images and final tomogram quality with the applied reconstruction protocol of systematically placed patches in high resolution compared to a reconstruction based on gold fiducials. Further, a fiducial free preparation was preferred to minimize possible artefacts due to gold fiducials within the AZ profile in tilt series of high magnification. All reconstructed tomograms were randomized by random number sampling prior to segmentation and 3D reconstruction. Segmentation and 3D reconstruction of electron tomograms were carried out in full resolution without binning using the 3Dmod software of the IMOD software package (Kremer et al., 1996). All types of SVs were annotated as ideal spherical objects by setting a point at the vesicle center in virtual section with its largest vesicle diameter using the drawing tool 'normal'. Further, the point was resized to the extent of the outer vesicle membrane using the mouse wheel in the drawing tool 'normal'. Within the reconstructed tomograms, we observed that SVs often deviate from an ideal spherical object and, despite possible deformation, were clearly distinguishable from smooth endoplasmatic reticulum. SVs of 0–200 nm euclidean distance to the presynaptic membrane were included into the annotation and defined as SV pool (Rollenhagen et al., 2007). SVs which were tethered or docked within the peri-synaptic area (lateral distance of 200 nm to AZ edge on the same virtual section, cf. mean AZ spacing at giant MFB AZs in rats: 0.40 (P28) - 0.48 μm (adult) (Rollenhagen et al., 2007)) and with a distance up to 10 nm to the plasma membrane were annotated as vesicles connected outside of the AZ. Presynaptic membranes (AZ profiles) were two-dimensionally annotated as 'open' line objects, of which gaps of 15–20 virtual sections were linearly interpolated using the tool 'interpolator'. The synaptic cleft volume was quantified via one or more separate 'closed' objects. Every 20 virtual section, the area between the inner part of the double lipid membranes of pre- and postsynapse was annotated and interpolated in between using the tool 'interpolator' and the 'smooth' function. If needed, contours were manually corrected after interpolation. The extent of the synaptic cleft was defined by the extent of postsynaptic filaments. To improve the illustration of SVs in the 3D tomograms, the following settings were uniformly used: grade 4 in global quality of points, option 'fill' in the 'drawing style'.

2D and 3D quantitative data evaluation

3D coordinates of SV centers and membranes, vesicle radii, and lengths of IMOD open and closed 'line' objects were extracted via command line using 'imodinfo' and 'model2point'. Individual 3D AZ surfaces contained one or more 2D AZ profiles (open 'line' objects) per virtual electron tomographic z-slice. Area and volume information of IMOD objects were assessed by using the 'mesh' function. To avoid inaccurate mesh calculation due to complex branched shapes of AZ surfaces, sub-meshes of presynaptic membranes and the synaptic cleft were calculated separately as distinct surfaces within one IMOD object. SVs of 0–10 nm distance to the AZ membrane and EDM connecting SV and presynaptic membrane were manually measured in 3Dmod. The main EDM width was measured in parallel to the AZ membrane profile at the virtual slice of the defined SV center. The existence of a main EDM was observed in nearly all SVs between 0 and 10 nm in the entire data set. SVs of 0–2 nm distance and connecting EDM to the presynaptic membrane were defined as tightly docked, SVs of 0–5 nm distance and connecting EDM to the presynaptic membrane were defined as docked. To avoid measuring artefacts, the 'slicer' window function was used to visualize the contact zone between SV and presynaptic membrane from different angles. 3D coordinates of SVs and membranes were processed via text files in Jupyter Notebook 6.2.0 (Anaconda), a web-based programming environment for Python (van Rossum and de Boer, 1991), Version 3.7, with a custom-written script. Stereogeometrical data were calculated using 'numpy' (Harris et al., 2020), 'scikit-learn' (Pedregosa et al., 2011) and 'shapely' (Gillies et al., 2007). Mathematical calculations are described in detail within the custom-written Python scripts. For 2D quantification of mitochondria within 0–500 nm distance to giant MFB AZ profiles and their perisynaptic membranes, a randomly placed systematic grid lattice with a point spacing of 22.36 nm was used as an overlay on electron micrographs of defined magnification (15,000×). Points were counted depending on their localization ('M' = mitochondria, 'NM' = no mitochondria) and categorized in five bands of 100 nm distance each to the membranes (0–100 nm, 100-200 nm etc.). 2D AZ profiles of RIM1$\alpha^{-/-}$ giant MFBs (N = 45) and controls (N = 20) were selected upon a clear presence of mitochondria near the AZ profile and excellent morphological ultrastructure of the giant MFB. In case of several AZs at a spine head, the AZ nearest to the mitochondrial accumulation was quantified. In case of the quantification at the perisynaptic membrane, mitochondria were only quantified in case they were clearly associated to the depicted one AZ profile and not ambiguously to nearby spaced AZ profiles at the same spine head. The counting method for 2D spatial stereology was modified from C. Hacker and J. Lucocq (Hacker and Lucocq, 2014).

QUANTIFICATION AND STATISTICAL ANALYSIS

Statistical analyses were carried out with the statistical software programs Sigma Plot 14 (Systat Software GmbH) and OriginPro 2021 (Origin Lab). Estimation statistics (linear mixed modeling, bootstrapping) were performed with Python 3.7 using 'statsmodels' 0.13.2 (http://conference.scipy.org/proceedings/scipy2010/pdfs/seabold.pdf). 2D stereology of mitochondria was carried out in Fiji Version v1.53 n (Schindelin et al., 2012). The number of animals and the sample size for tomograms was defined *a priori* according to standard publications in electron tomography (Fernandez-Busnadiego et al., 2013; Imig et al., 2014). The experimental procedure was independently replicated several times within the laboratory. Asterisks in figures indicate the level of significance (*p < 0.05, **p < 0.01, ***p < 0.001), n/N is used as abbreviation for the sample number. For all data, normality was tested using Shapiro-Wilk tests (sample size N $\leq$ 5000) and Kolmogorov-Smirnov-tests. For comparison of two groups, non-parametric data were analyzed

using non-parametric Mann-Whitney rank sum tests and parametric data using Welch's t-tests. The power (PW) of conducted analyses is reported separately. For both groups, non-equal variances were assumed due to the highly experimental character of observed (rare) phenomena (e.g., tightly docked SVs). Correlations were calculated using the Spearman rank order correlation. Comparison of data distributions were calculated using the Akaike information criterion and the F-test. For comparison of three groups, non-parametric data were analyzed using a Kruskal-Wallis ANOVA (Figure S2). Data are reported as median $\pm 25^{th}$ and 75th percentile for non-parametric data, unless indicated otherwise, and as mean ± SD for parametric data. In boxplots, horizontal lines represent median values, dashed lines represent mean values. Further, boxes quartiles and whiskers represent 10th and 90th percentiles. Scatterplots show individual data points unless indicated otherwise. All plots were produced with OriginPro 2021 except plots for Figure S2B-E which were created using Matplotlib. Figures were assembled using Adobe Illustrator 2021 (Adobe Creative Cloud). Table S1 contains all numerical values not stated in text and figure legends including p values and sample sizes.

Data availability
The datasets and computer codes produced in this study are available upon request.